Detection of X-Ray Polarization from the Blazar 1ES 1959+650 with the Imaging X-Ray Polarimetry Explorer

Manel Errando, Ioannis Liodakis, Alan P. Marscher, Herman L. Marshall, Riccardo Middei, Michela Negro, Abel Lawrence Peirson, Matteo Perri, Simonetta Puccetti, Pazit L. Rabinowitz, et al.

The Astrophysical Journal, 963:5 (13pp), 2024 March 1 https://doi.org/10.3847/1538-4357/ad1ce4

Detection of X-Ray Polarization from the Blazar 1ES 1959+650 with the Imaging X-Ray Polarimetry Explorer

Manel Errando[1], Ioannis Liodakis[2,3], Alan P. Marscher[4], Herman L. Marshall[5], Riccardo Middei[6,7], Michela Negro[8], Abel Lawrence Peirson[9], Matteo Perri[6,7], Simonetta Puccetti[6], Pazit L. Rabinowitz[1], Iván Agudo[10], Svetlana G. Jorstad[4,11], Sergey S. Savchenko[11,12], Dmitry Blinov[13,14], Ioakeim G. Bourbah[14], Sebastian Kiehlmann[13,14], Evangelos Kontopodis[14], Nikos Mandarakas[13,14], Stylianos Romanopoulos[13,14], Raphael Skalidis[13,14,15], Anna Vervelaki[14], Francisco José Aceituno[10], Maria I. Bernardos[10], Giacomo Bonnoli[10,16], Víctor Casanova[10], Beatriz Agís-González[10], César Husillos[10,17], Alessandro Marchini[18], Alfredo Sota[10], Pouya M. Kouch[2,19], Elina Lindfors[2], Carolina Casadio[13,14], Juan Escudero[20], Ioannis Myserlis[21,22], Ryo Imazawa[23], Mahito Sasada[24], Yasushi Fukazawa[23,25,26], Koji S. Kawabata[23,25,26], Makoto Uemura[23,25,26], Tsunefumi Mizuno[25], Tatsuya Nakaoka[25], Hiroshi Akitaya[25,27], Mark Gurwell[28], Garrett K. Keating[28], Ramprasad Rao[28], Adam Ingram[29,30], Francesco Massaro[31,32], Lucio Angelo Antonelli[6,7], Raffaella Bonino[31,32], Elisabetta Cavazzuti[33], Chien-Ting Chen[34], Nicolò Cibrario[31,32], Stefano Ciprini[6,35], Alessandra De Rosa[36], Laura Di Gesu[33], Federico Di Pierro[31], Immacolata Donnarumma[33], Steven R. Ehlert[3], Francesco Fenu[37], Ephraim Gau[1], Vladimir Karas[38], Dawoon E. Kim[36,39,40], Henric Krawczynski[1], Marco Laurenti[6,35], Lindsey Lisalda[1], Rubén López-Coto[20], Grzegorz Madejski[9], Frédéric Marin[41], Andrea Marinucci[33], Ikuyuki Mitsuishi[42], Fabio Muleri[36], Luigi Pacciani[36], Alessandro Paggi[32], Pierre-Olivier Petrucci[43], Nicole Rodriguez Cavero[1], Roger W. Romani[9], Fabrizio Tavecchio[16], Stefano Tugliani[31,32], Kinwah Wu[44], Matteo Bachetti[45], Luca Baldini[46,47], Wayne H. Baumgartner[3], Ronaldo Bellazzini[46], Stefano Bianchi[48], Stephen D. Bongiorno[3], Alessandro Brez[46], Niccolò Bucciantini[49,50,51], Fiamma Capitanio[36], Simone Castellano[46], Enrico Costa[36], Ettore Del Monte[36], Niccolò Di Lalla[9], Alessandro Di Marco[36], Victor Doroshenko[52], Michal Dovčiak[38], Teruaki Enoto[53], Yuri Evangelista[36], Sergio Fabiani[36], Riccardo Ferrazzoli[36], Javier A. Garcia[54], Shuichi Gunji[55], Kiyoshi Hayashida[56], Jeremy Heyl[57], Wataru Iwakiri[58], Philip Kaaret[3], Fabian Kislat[59], Takao Kitaguchi[53], Jeffery J. Kolodziejczak[3], Fabio La Monaca[36,39,40], Luca Latronico[31], Simone Maldera[31], Alberto Manfreda[60], Giorgio Matt[48], C.-Y. Ng[61], Stephen L. O'Dell[3], Nicola Omodei[9], Chiara Oppedisano[31], Alessandro Papitto[7], George G. Pavlov[62], Melissa Pesce-Rollins[46], Maura Pilia[45], Andrea Possenti[45], Juri Poutanen[19], Brian D. Ramsey[3], John Rankin[36], Ajay Ratheesh[36], Oliver J. Roberts[34], Carmelo Sgrò[46], Patrick Slane[28], Paolo Soffitta[36], Gloria Spandre[46], Douglas A. Swartz[34], Toru Tamagawa[53], Roberto Taverna[63], Yuzuru Tawara[42], Allyn F. Tennant[3], Nicholas E. Thomas[3], Francesco Tombesi[35,40,64], Alessio Trois[45], Sergey S. Tsygankov[19], Roberto Turolla[44,63], Jacco Vink[65], Martin C. Weisskopf[3], Fei Xie[36,66], and Silvia Zane[44]

[1] Physics Department and McDonnell Center for the Space Sciences, Washington University in St. Louis, St. Louis, MO 63130, USA; errando@wustl.edu
[2] Finnish Centre for Astronomy with ESO, FI-20014 University of Turku, Finland
[3] NASA Marshall Space Flight Center, Huntsville, AL 35812, USA
[4] Institute for Astrophysical Research, Boston University, 725 Commonwealth Avenue, Boston, MA 02215, USA
[5] MIT Kavli Institute for Astrophysics and Space Research, Massachusetts Institute of Technology, 77 Massachusetts Avenue, Cambridge, MA 02139, USA
[6] Space Science Data Center, Agenzia Spaziale Italiana, Via del Politecnico snc, I-00133 Roma, Italy
[7] INAF Osservatorio Astronomico di Roma, Via Frascati 33, I-00078 Monte Porzio Catone (RM), Italy
[8] Department of Physics and Astronomy, Louisiana State University, Baton Rouge, LA 70803, USA
[9] Department of Physics and Kavli Institute for Particle Astrophysics and Cosmology, Stanford University, Stanford, CA 94305, USA
[10] Instituto de Astrofísica de Andalucía (CSIC), Apartado 3004, E-18080 Granada, Spain
[11] Saint Petersburg State University, 7/9 Universitetskaya nab., St. Petersburg, 199034 Russia
[12] Pulkovo Observatory, St. Petersburg, 196140, Russia
[13] Institute of Astrophysics, Foundation for Research and Technology-Hellas, GR-70013 Heraklion, Greece
[14] Department of Physics, University of Crete, 70013, Heraklion, Greece
[15] Owens Valley Radio Observatory, California Institute of Technology, MC 249-17, Pasadena, CA 91125, USA
[16] INAF Osservatorio Astronomico di Brera, Via E. Bianchi 46, I-23807 Merate (LC), Italy
[17] Geological and Mining Institute of Spain (IGME-CSIC), Calle Ríos Rosas 23, E-28003, Madrid, Spain
[18] University of Siena, Astronomical Observatory, Via Roma 56, I-53100 Siena, Italy
[19] Department of Physics and Astronomy, FI-20014 University of Turku, Finland
[20] Instituto de Astrofísica de Andalucía-CSIC, Glorieta de la Astronomía s/n, E-18008, Granada, Spain
[21] Institut de Radioastronomie Millimétrique, Avenida Divina Pastora, 7, Local 20, E-18012 Granada, Spain
[22] Max-Planck-Institut für Radioastronomie, Auf dem Hügel 69, D-53121 Bonn, Germany
[23] Department of Physics, Graduate School of Advanced Science and Engineering, Hiroshima University, Kagamiyama, 1-3-1 Higashi-Hiroshima, Hiroshima 739-8526, Japan
[24] Department of Physics, Tokyo Institute of Technology, 2-12-1 Ookayama, Meguro-ku, Tokyo 152-8551, Japan
[25] Hiroshima Astrophysical Science Center, Hiroshima University, 1-3-1 Kagamiyama, Higashi-Hiroshima, Hiroshima 739-8526, Japan
[26] Core Research for Energetic Universe (Core-U), Hiroshima University, 1-3-1 Kagamiyama, Higashi-Hiroshima, Hiroshima 739-8526, Japan
[27] Planetary Exploration Research Center, Chiba Institute of Technology, 2-17-1 Tsudanuma, Narashino 275-0016, Japan
[28] Center for Astrophysics | Harvard & Smithsonian, 60 Garden Street, Cambridge, MA 02138, USA
[29] Department of Physics—Astrophysics, University of Oxford, Denys Wilkinson Building, Keble Road, Oxford OX1 3RH, UK
[30] School of Mathematics, Statistics and Physics, Newcastle University, Herschel Building, Newcastle upon Tyne, NE1 7RU, UK
[31] Istituto Nazionale di Fisica Nucleare, Sezione di Torino, Via Pietro Giuria 1, I-10125 Torino, Italy
[32] Dipartimento di Fisica, Università degli Studi di Torino, Via Pietro Giuria 1, I-10125 Torino, Italy
[33] ASI—Agenzia Spaziale Italiana, Via del Politecnico snc, I-00133 Roma, Italy

[34] Science and Technology Institute, Universities Space Research Association, Huntsville, AL 35805, USA
[35] Istituto Nazionale di Fisica Nucleare, Sezione di Roma "Tor Vergata", Via della Ricerca Scientifica 1, I-00133 Roma, Italy
[36] INAF Istituto di Astrofisica e Planetologia Spaziali, Via del Fosso del Cavaliere 100, I-00133 Roma, Italy
[37] Karlsruhe Institute of Technology (KIT), Institute for Astroparticle Physics, Karlsruhe, Germany
[38] Astronomical Institute of the Czech Academy of Sciences, Boční II 1401/1, 14100 Praha 4, Czech Republic
[39] Dipartimento di Fisica, Università degli Studi di Roma "La Sapienza", Piazzale Aldo Moro 5, I-00185 Roma, Italy
[40] Dipartimento di Fisica, Università degli Studi di Roma "Tor Vergata", Via della Ricerca Scientifica 1, I-00133 Roma, Italy
[41] Université de Strasbourg, CNRS, Observatoire Astronomique de Strasbourg, UMR 7550, F-67000 Strasbourg, France
[42] Graduate School of Science, Division of Particle and Astrophysical Science, Nagoya University, Furo-cho, Chikusa-ku, Nagoya, Aichi 464-8602, Japan
[43] Université Grenoble Alpes, CNRS, IPAG, F-38000 Grenoble, France
[44] Mullard Space Science Laboratory, University College London, Holmbury St Mary, Dorking, Surrey RH5 6NT, UK
[45] INAF Osservatorio Astronomico di Cagliari, Via della Scienza 5, I-09047 Selargius (CA), Italy
[46] Istituto Nazionale di Fisica Nucleare, Sezione di Pisa, Largo B. Pontecorvo 3, I-56127 Pisa, Italy
[47] Dipartimento di Fisica, Università di Pisa, Largo B. Pontecorvo 3, I-56127 Pisa, Italy
[48] Dipartimento di Matematica e Fisica, Università degli Studi Roma Tre, Via della Vasca Navale 84, I-00146 Roma, Italy
[49] INAF Osservatorio Astrofisico di Arcetri, Largo Enrico Fermi 5, I-50125 Firenze, Italy
[50] Dipartimento di Fisica e Astronomia, Università degli Studi di Firenze, Via Sansone 1, I-50019 Sesto Fiorentino (FI), Italy
[51] Istituto Nazionale di Fisica Nucleare, Sezione di Firenze, Via Sansone 1, I-50019 Sesto Fiorentino (FI), Italy
[52] Institut für Astronomie und Astrophysik, Universität Tübingen, Sand 1, D-72076 Tübingen, Germany
[53] RIKEN Cluster for Pioneering Research, 2-1 Hirosawa, Wako, Saitama 351-0198, Japan
[54] NASA Goddard Space Flight Center, Greenbelt, MD 20771, USA
[55] Yamagata University,1-4-12 Kojirakawa-machi, Yamagata-shi 990-8560, Japan
[56] Osaka University, 1-1 Yamadaoka, Suita, Osaka 565-0871, Japan
[57] University of British Columbia, Vancouver, BC V6T 1Z4, Canada
[58] International Center for Hadron Astrophysics, Chiba University, Chiba 263-8522, Japan
[59] Department of Physics and Astronomy and Space Science Center, University of New Hampshire, Durham, NH 03824, USA
[60] Istituto Nazionale di Fisica Nucleare, Sezione di Napoli, Strada Comunale Cinthia, I-80126 Napoli, Italy
[61] Department of Physics, The University of Hong Kong, Pokfulam, Hong Kong
[62] Department of Astronomy and Astrophysics, Pennsylvania State University, University Park, PA 16802, USA
[63] Dipartimento di Fisica e Astronomia, Università degli Studi di Padova, Via Marzolo 8, I-35131 Padova, Italy
[64] Department of Astronomy, University of Maryland, College Park, MD 20742, USA
[65] Anton Pannekoek Institute for Astronomy & GRAPPA, University of Amsterdam, Science Park 904, 1098 XH Amsterdam, The Netherlands
[66] Guangxi Key Laboratory for Relativistic Astrophysics, School of Physical Science and Technology, Guangxi University, Nanning 530004, People's Republic of China

Received 2023 November 28; revised 2023 December 27; accepted 2024 January 8; published 2024 February 21

Abstract

Observations of linear polarization in the 2–8 keV energy range with the Imaging X-ray Polarimetry Explorer (IXPE) explore the magnetic field geometry and dynamics of the regions generating nonthermal radiation in relativistic jets of blazars. These jets, particularly in blazars whose spectral energy distribution peaks at X-ray energies, emit X-rays via synchrotron radiation from high-energy particles within the jet. IXPE observations of the X-ray-selected BL Lac–type blazar 1ES 1959+650 on 2022 May 3–4 showed a significant linear polarization degree of $\Pi_x = 8.0\% \pm 2.3\%$ at an electric-vector position angle $\psi_x = 123° \pm 8°$. However, on 2022 June 9–12, only an upper limit of $\Pi_x \leqslant 5.1\%$ could be derived (at the 99% confidence level). The degree of optical polarization at that time, $\Pi_O \sim 5\%$, is comparable to the X-ray measurement. We investigate possible scenarios for these findings, including temporal and geometrical depolarization effects. Unlike some other X-ray-selected BL Lac objects, there is no significant chromatic dependence of the measured polarization in 1ES 1959+650, and its low X-ray polarization may be attributed to turbulence in the jet flow with dynamical timescales shorter than 1 day.

Unified Astronomy Thesaurus concepts: Relativistic jets (1390); X-ray active galactic nuclei (2035); Active galactic nuclei (16); Blazars (164); Polarimetry (1278); Spectropolarimetry (1973)

1. Introduction

Relativistic jets are powerful streams of collimated plasma and radiation that play a prominent role in various astrophysical phenomena, such as active galactic nuclei (AGN), γ-ray bursts, and X-ray binary systems (Begelman et al. 1984; Falcke et al. 2004; Hughes & Bregman 2006; Blandford et al. 2019). In the case of blazars, these jets are fueled by accretion onto a central supermassive black hole within an AGN and are oriented in a direction that is closely aligned with Earth's line of sight (Urry & Padovani 1995). These jets accelerate particles to energies beyond 10^{10} eV, producing nonthermal emission observed across a wide range of frequencies, from radio to very high-energy (>0.1 TeV) γ-rays (Giommi et al. 2012; Liodakis et al. 2019). Advancements in understanding the physics of relativistic jets rely heavily on multiwavelength observations encompassing the spectral energy distribution, flux variability, and polarization of the observed emission.

According to most theoretical models for the production, acceleration, and collimation of relativistic jets, the plasma is Poynting-flux-dominated close to the black hole, where the jet is accelerated and collimated (e.g., Blandford & Znajek 1977; Vlahakis & Königl 2004). Near the end of the acceleration and collimation zone, there is a transition to a particle-dominated flow (e.g., Lyubarsky 2010). It is currently unclear, however, where most of the particle acceleration and radiative dissipation take place. Multiple processes could play major roles in energizing the particles that produce the radiation in blazar jets.

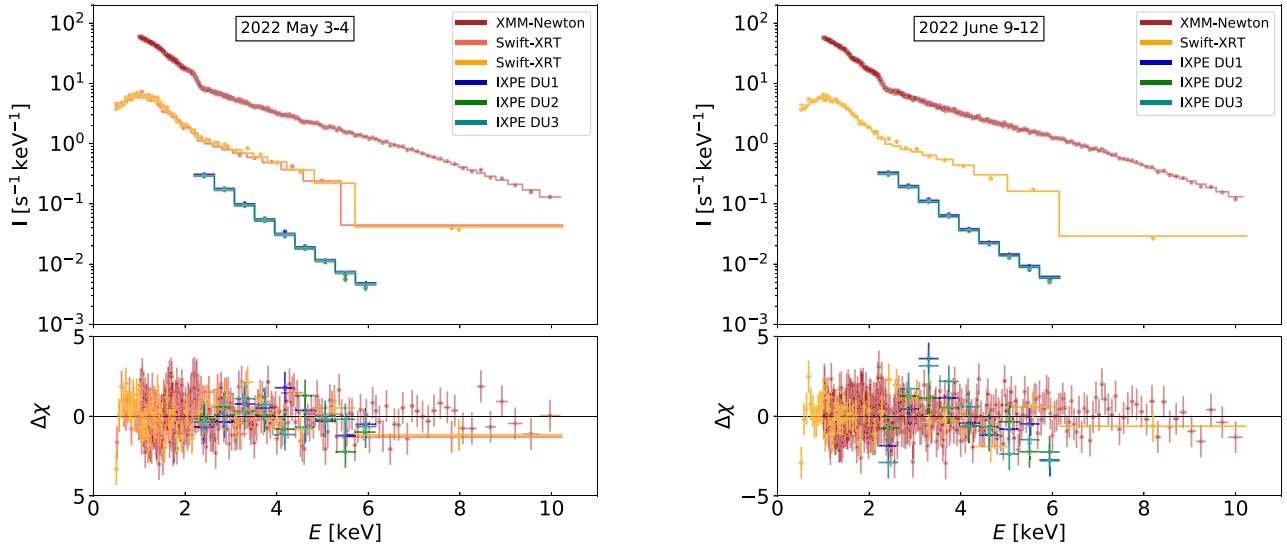

Figure 1. Spectral fit to the X-ray data of 1ES 1959+650 during IXPE observations on 2022 May 3–4 (left panel) and 2022 June 9–12 (right panel). The IXPE Stokes *I*, Swift-XRT, and XMM-Newton spectra are fit to derive the column density absorption and determine the presence of spectral curvature. These results will be used in the later spectropolarimetric fit of the IXPE *I*, *Q*, and *U* spectra.

These include magnetic reconnection events (e.g., Romanova & Lovelace 1992; Kagan et al. 2015; Werner et al. 2018), relativistic shocks (e.g., Blandford & Ostriker 1978; Nishikawa et al. 2003; Sironi et al. 2015a), and stochastic particle acceleration (e.g., Dermer et al. 1996; Kirk et al. 1996; Katarzyński et al. 2006). These mechanisms can efficiently accelerate particles, although particle-in-cell simulations find that magnetic reconnection is more efficient than shocks at doing so where the magnetization level is high (Sironi & Spitkovsky 2014). On the other hand, shocks can be more efficient in regions where the magnetization is low (Sironi et al. 2015b).

Multiwavelength observations of linear polarization probe the geometry of the magnetic field in different locations in relativistic jets (e.g., Angel & Stockman 1980; Jorstad et al. 2005; Marscher & Jorstad 2021). The results can indicate which of the particle acceleration mechanisms are operating in sites of strong high-energy radiation (e.g., Zhang et al. 2019, 2022; Tavecchio 2021; Di Gesu et al. 2022b; Marscher & Jorstad 2022). Such polarization observations of blazars have long been available at radio, infrared, and optical wavelengths. Observations in the X-ray band now benefit from the availability of linear polarization sensitivity through the Imaging X-ray Polarimetry Explorer (IXPE) satellite (Weisskopf et al. 2022), which began science operations on 2022 January 11. IXPE consists of three 4 m focal length X-ray mirrors that focus on three identical polarization-sensitive gas pixel detector units (DU1–3). The sensitivity of an X-ray polarimeter is commonly assessed by its minimum detectable polarization at a 99% confidence level, MDP_{99}. At a flux level of $F_{2-8\,\mathrm{keV}} = 10^{-10}$ erg cm^{-2} s^{-1}, IXPE achieves $\mathrm{MDP}_{99} \approx 8\%$ in a 50 ks exposure.

The BL Lacertae object 1ES 1959+650 ($z = 0.047$; de Vaucouleurs et al. 1991) stands out as one of the brightest X-ray blazars. Only four BL Lac objects in the Einstein Slew Survey exhibit a higher X-ray flux (Perlman et al. 1996). It is also among the first blazars from which TeV γ-rays have been detected (Holder et al. 2003). The X-ray flux of 1ES 1959+650 generally exceeds 10^{-10} erg cm^{-2} s^{-1} in the 0.1–10 keV range, displaying variability on timescales of <1 hr (Kapanadze et al. 2014). While X-ray and γ-ray fluxes are generally found to be correlated, a notable "orphan" TeV flare without an X-ray counterpart was detected by the Whipple observatory in 2002 (Krawczynski et al. 2004). Owing to its bright X-ray emission, 1ES 1959+650 was among the first blazars observed by IXPE.

The radio-to-X-ray emission from 1ES 1959+650 is commonly interpreted as originating from synchrotron radiation by relativistic electrons cooling in the jet's magnetic field. Synchrotron radiation is inherently polarized. The expected degree of polarization from a power-law energy spectrum of relativistic electrons $N(E_e) \propto E_e^{-s}$ in a homogeneous magnetic field is $\Pi = (s+1)/(s+7/3) \approx 70\%$ for $s \approx 2$ (Rybicki & Lightman 1979). If the magnetic field configuration has a random component B_r, then the polarization degree will be suppressed by a factor $B_0^2/(B_0^2 + B_r^2)$, where B_0 is the intensity of the ordered magnetic field component (Ginzburg & Syrovatskii 1965). In blazars, the presence of a random component in the magnetic field reduces the polarization signal from a maximum value of order 75% to an average value that is usually between a few and tens of percent (e.g., Blinov et al. 2021; Marscher & Jorstad 2021). Therefore, polarization measurements in the X-ray band by IXPE are sensitive to the relative ratio of the random to the ordered magnetic field in the region of the jet where the nonthermal emission from the highest-energy particles is emitted. This new probe of the magnetic field intensity and geometry in relativistic jets can be used to discern among the possible models for particle acceleration. For instance, if acceleration occurs in stationary shocks, downstream of which particles lose energy, we anticipate steady X-ray emission with higher polarization than the polarization of the optical emission by lower-energy particles radiating over a larger volume (Angelakis et al. 2016; Tavecchio et al. 2018, 2020; Di Gesu et al. 2022b; Marscher & Jorstad 2022; Zhang et al. 2022). Conversely, magnetic reconnection events convert magnetic energy into kinetic energy, resulting in moderate X-ray and optical

Table 1
Summary and Results from IXPE, XMM-Newton, and Swift-XRT X-Ray Observations on 2022 May 3–4 and June 9–12

Telescope	Energy Range (keV)	ObsID	Date	Exposure (ks)	$F_{2-8\ \mathrm{keV}}$ (10^{-10} erg cm^{-2} s^{-1})	Γ_x	χ^2/dof
2022 May 3–4							
IXPE	2.0–8.0	01006201	2022 05 03–04	54	1.24 ± 0.02	2.50 ± 0.02	30.6/26
Swift-XRT	0.5–10	00096560006	2022 05 03	0.9	1.57 ± 0.04	2.18 ± 0.04	314/349
Swift-XRT	0.5–10	00096560007	2022 05 04	0.9	1.63 ± 0.05	2.17 ± 0.04	374/351
XMM-Newton	1.0–10	0902110801	2022 05 06	16	1.35 ± 0.01	2.26 ± 0.01	196/155
2022 June 9–12							
IXPE	2.0–8.0	01006001	2022 06 09–12	200	1.47 ± 0.01	2.29 ± 0.01	36.5/25
Swift-XRT	0.5–10	00096560012	2022 06 12	0.9	2.23 ± 0.05	2.20 ± 0.04	334/344
XMM-Newton	1.0–10	0902111201	2022 06 23	18	1.34 ± 0.01	2.20 ± 0.01	195/155

polarization, with a weaker dependence on photon energy (e.g., Bodo et al. 2021; Zhang et al. 2022).

Here we present the first detection of linear X-ray polarization from 1ES 1959+650 by IXPE on 2022 May 3–4 and June 9–12. We describe the IXPE measurements, as well as X-ray spectral observations with the Neil Gehrels Swift X-ray Telescope (Swift-XRT) and XMM-Newton, in Section 2 and observations at other wave bands in Section 3. We discuss and interpret the results in Section 4 and summarize our findings in Section 5.

2. X-Ray Observations

IXPE first observed 1ES 1959+650 on 2022 May 3–4 with an exposure time of 54 ks. A second science observation was carried out on 2022 June 9–12, accumulating 200 ks of exposure. XMM-Newton (Strüder et al. 2001) collected two contemporaneous exposures of 1ES 1959+650, and Swift-XRT (Burrows et al. 2005) monitored the source with a total of 11 exposures during the duration of the campaign.

We combine the IXPE Stokes *I*, Swift-XRT, and XMM-Newton spectra to characterize the energy spectrum of 1ES 1959+650 in the X-ray band. The goal of this combined fit is to determine the column density absorption and spectral shape of the X-ray spectrum of 1ES 1959+650, as the 2–8 keV energy range of IXPE is too narrow to robustly measure the level of neutral density absorption and the potential presence of spectral curvature. The flux normalizations and spectral properties are left free to allow for intercalibration uncertainties (Madsen et al. 2017) as well as flux and spectral variability on timescales of days, which is often observed in 1ES 1959+650 even in relatively quiescent X-ray states (Tagliaferri et al. 2008). The fit of the combined data set to an absorbed power law $dN/dE \propto E^{-\Gamma_x}$ yields a χ^2/dof fit statistic of 554/497 (with associated probability $p = 0.04$) for the May 3–4 data and 616/566 ($p = 0.07$) for June 9–12 (Figure 1). The best-fit parameters describing the spectra are listed in Table 1. Changing the model to an absorbed log-parabola does not significantly improve the fit in either case. The derived column density of $(1.32 \pm 0.04) \times 10^{21}$ cm^{-2}, exceeding the Galactic value by 30% (HI4PI Collaboration et al. 2016), suggests the presence of additional neutral absorption along the line of sight within the host galaxy to the object, consistent with previous studies (Aliu et al. 2013, 2014). During both epochs, the average X-ray flux is within 10% of the median value measured by Swift-XRT between 2005 and 2022 (Figure 2; Stroh & Falcone 2013). We conclude that 1ES 1959+650 was in an average X-ray flux state during the IXPE campaign.

We have searched for time-averaged X-ray polarization from 1ES 1959+650 in the IXPE data. First, the *I* spectra were fit with an absorbed power-law model. The absorbing column density was fixed to the value obtained during the combined spectral fit, but the power-law normalization and photon index were allowed to vary. We then tested for the presence of a constant degree of polarization and angle as a function of energy by performing a spectropolarimetric fit to the Stokes *I*, *Q*, and *U* spectra, with the only free parameters being the degree of polarization and polarization angle (Figure 3).

On May 3–4, the spectrum obtained from IXPE displayed a softer photon index of $\Gamma = 2.50 \pm 0.02$ compared to the contemporaneous XMM-Newton and Swift-XRT data (Table 1). On June 9–12, the IXPE-derived $\Gamma = 2.29 \pm 0.01$ was in closer agreement with the value previously derived. The effect is likely to be the result of an improvement in the telescope alignment between the two observations. The polarization degree on May 3–4 was $\Pi_x = 8.0\% \pm 2.3\%$, with an electric-vector position angle $\psi_x = 123° \pm 8°$. A null hypothesis of no linear polarization can be excluded at a 3.5 σ confidence level. No significant linear polarization was detected on June 9–12. From this second IXPE observation, we derive an upper limit of $\Pi_x < 5.1\%$ (99% confidence level), with the polarization angle left unconstrained. The hypothesis that the degree of polarization remained constant across the May 3–4 and June 9–12 IXPE observations has an associated probability of $P = 0.0244$ using a χ^2 test; i.e., it can only be excluded at a 2.3σ level.

To search for time-dependent X-ray polarization, we split the 200 ks duration IXPE exposure from June 9–12 into four 50 ks slices and repeated the spectropolarimetric fit described above independently for each time bin. We found no significant linear polarization in three out of the four segments, with only the third one showing significant polarization corresponding to a 2.8 σ posttrial confidence level (Figure 2). The constraints on the degree of polarization in the four time bins are $\Pi_x < 6.0\%$, $<10.2\%$, $7.5\% \pm 2.3\%$, and $<7.6\%$ (upper limits are 99% confidence level). The polarization angle is only constrained for the third time bin to be $\psi_x = 127° \pm 9°$.

X-ray data reduction procedures are detailed in Appendix A.

3. Radio, Infrared, and Optical Observations

Figure 2 summarizes the time evolution of the X-ray and optical polarization measurements of 1ES 1959+650. Contemporaneous polarization observations were obtained at radio (millimeter), infrared (IR), and optical wavelengths using the

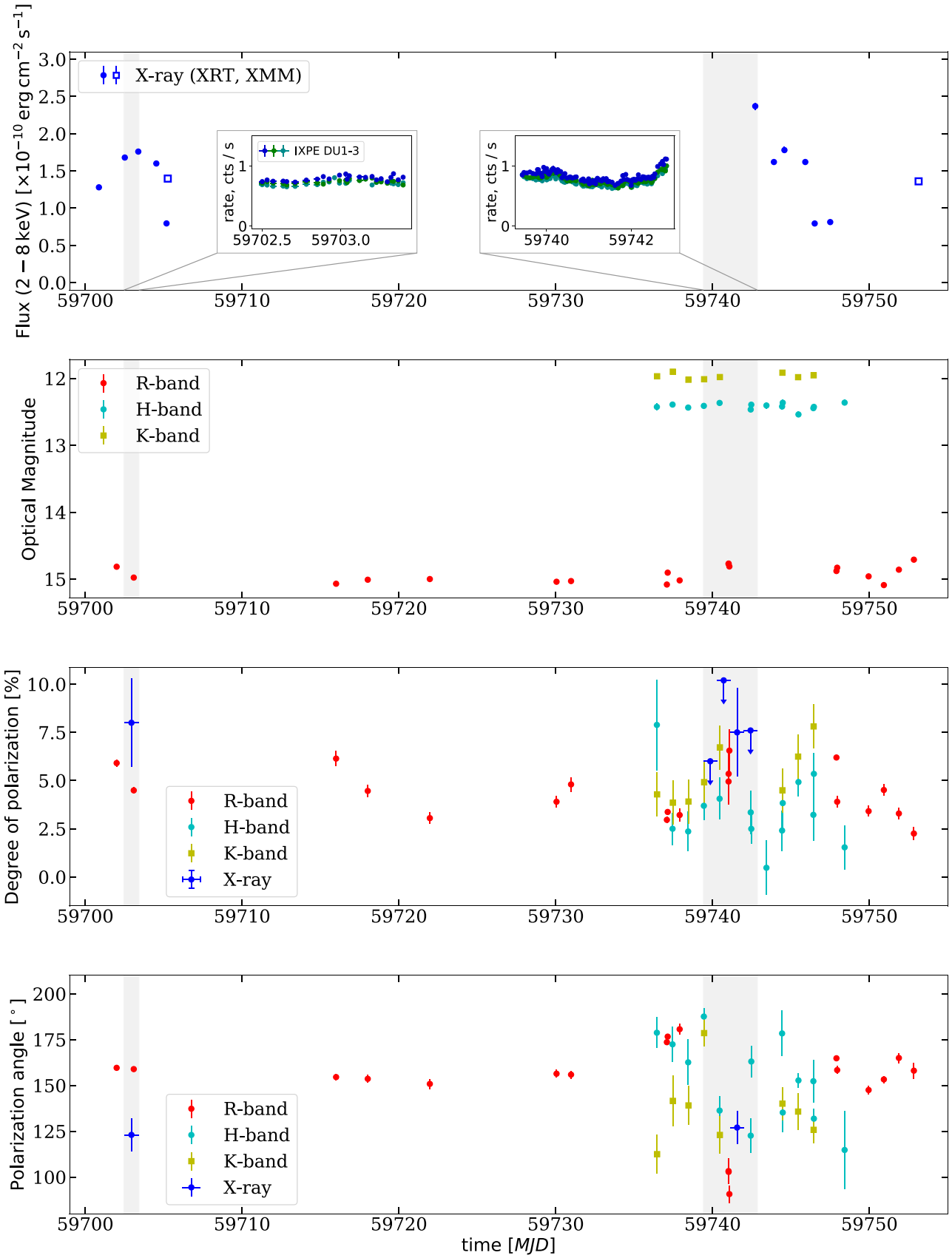

Figure 2. X-ray, optical, and IR light curves contemporaneous with the IXPE observations of 1ES 1959+650. Observations are described in Sections 2 and 3. Panels show, from top to bottom, X-ray flux, optical and IR brightness in magnitudes, degree of polarization, and polarization angle. Inset plots in the top panel display the X-ray light curve measured by IXPE. Blue data points represent significant measurements of X-ray polarization, while blue downward-pointing arrows indicate 99% confidence level upper limits during time periods without a significant detection of X-ray polarization. Gray vertical shaded areas indicate the two epochs of observation of IXPE.

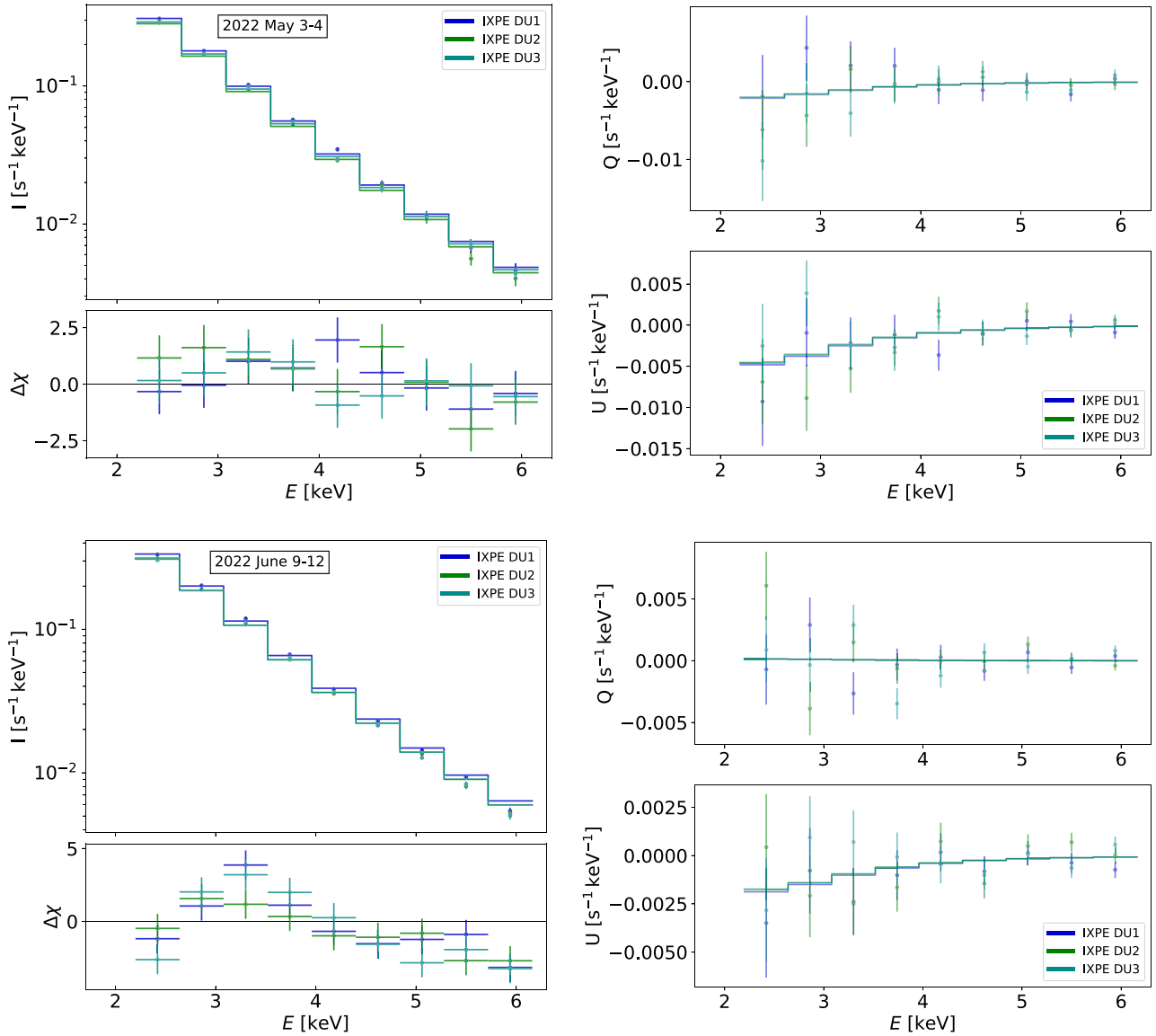

Figure 3. Spectropolarimetric fit to the X-ray data of 1ES 1959+650 during IXPE observations on 2022 May 3–4 (top panels) and 2022 June 9–12 (bottom panels). Panels on the left present the fit to the IXPE Stokes I with its residuals, while panels on the right show the fits to the IXPE Q and U spectra.

Institut de Radioastronomie Millimétrique (IRAM) 30 m radio telescope, the 1.8 m Perkins Telescope (PTO), the Calar Alto Observatory, the KANATA telescope, the Nordic Optical Telescope (NOT), the Sierra Nevada Observatory, RoboPol mounted at the 1.3 m telescope of the Skinakas Observatory, the Submillimeter Array (SMA), and the Very Long Baseline Array (VLBA).

Images of 1ES 1959+650 obtained at 7 mm (43 GHz) from VLBA data feature a ∼1 mas jet extending to the southeast of a compact "core" along a position angle of $\phi \sim 150°$ (Piner et al. 2010; Weaver et al. 2022). Figure 4 presents VLBA images at three epochs near the IXPE pointings obtained as part of the BEAM-ME monitoring project.[67] The data were obtained and analyzed using standard procedures, as described by Jorstad et al. (2017). We measure the linear polarization of the core to be $P_{\rm core} = 2.3\% \pm 0.2\%$ along $\psi_{\rm core} = 173° \pm 10°$ on 2022 June 5 and $P_{\rm core} = 2.8\% \pm 0.3\%$ along $\psi_{\rm core} = 152° \pm 10°$ on 2022 June 24. We determine only an upper limit to the degree of polarization of $P_{\rm core} \leqslant 2.4\%$ on 2022 April 30. When the resolved 43 GHz emission is included, the degree of polarization decreases to $P = 1.5\% \pm 0.5\%$ and $1.7\% \pm 0.9\%$ on June 5 and 24, respectively.

The IRAM observations were obtained during the first IXPE observation on 2022 May 5 (MJD 59705.0138) and during the second observation on 2022 June 12 (MJD 59742.9538) at 86.24 and 228.93 GHz under the Polarimetric Monitoring of AGN at Millimeter Wavelengths (POLAMI) Large Program[68] (Agudo et al. 2018a, 2018b; Thum et al. 2018). For the first observation, we obtained a 99% upper limit of $\Pi_{\rm R} < 8\%$ for the polarization degree at 228 GHz. During the second IXPE measurement, the IRAM observations yielded upper limits of $\Pi_{\rm R} < 1.6\%$ and $<9.6\%$ at 86 and 228 GHz, respectively.

SMA observations were obtained between the two IXPE exposures on 2022 June 1 (MJD 59731.60152) and 2022 June

[67] www.bu.blazars/BEAM-ME.html

[68] http://polami.iaa.es/

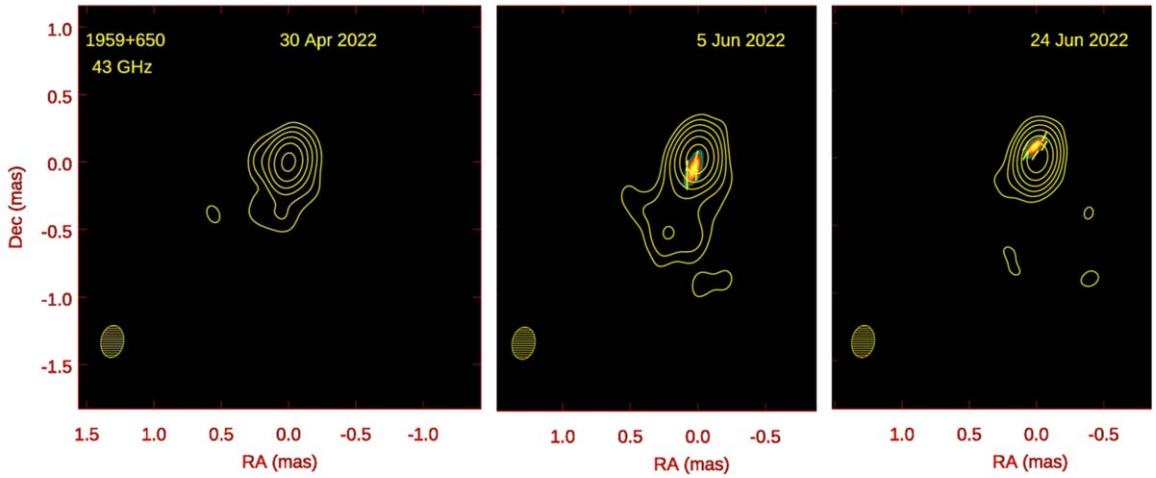

Figure 4. VLBA images of 1ES 1959+650 at 7 mm at three epochs contemporaneous with the IXPE observations. Contours: total intensity in factors of 2, starting at 2% of the peak intensity of (left to right) 0.16, 0.12, and 0.14 Jy beam^{-1}. Color coding: relative linearly polarized intensity, with maxima of (left to right) <4, 2.8, and 4.0 mJy beam^{-1}. Yellow line segments: electric-vector position angle of polarization. Cross-hatched ellipse in the lower left of each panel: FWHM of the elliptical restoring beam corresponding to the angular resolution along different directions. All positions are relative to the location of maximum intensity.

6 (MJD 59736.71253) at 225.3 GHz within the SMA Monitoring of AGNs with POLarization program. Data were taken with the SMA polarimeter (Marrone & Rao 2008) in full polarization mode using the SWARM correlator (Primiani et al. 2016). MWC 349 A and Callisto were used as the total flux calibrators and 3C 286 as the polarization calibrator. We find a low degree of polarization $\Pi_R = 1.92\% \pm 0.58\%$ along $\psi_R = 129^\circ \pm 8^\circ$ for the first observation, and $\Pi_R = 2.53\% \pm 0.5\%$ along $\psi_R = 156^\circ \pm 5^\circ$ for the second one.

IR photometric and polarimetric data in the H (1.6 μm) and K (2.2 μm) bands during the June 9–12 IXPE exposures were obtained using the MIMIR camera[69] at the PTO (Flagstaff, Arizona), operated by Boston University. The average and standard deviation of the host-corrected IR polarization degree were found to be $\Pi_H = 3.27\% \pm 0.16\%$ along a polarization angle $\psi_H = 162^\circ \pm 25^\circ$ and $\Pi_K = 4.73\% \pm 0.75\%$ along $\psi_K = 151^\circ \pm 28^\circ$.

During the first IXPE observation, we only have a single optical measurement from NOT, which yielded an optical polarization degree $\Pi_O = 4.49\% \pm 0.17\%$ along $\psi_O = 159^\circ \pm 1^\circ$. During the second IXPE observation, the median and standard deviation of the optical polarization degree was $\Pi_O = 5.4\% \pm 1.1\%$ along $\psi_O = 103^\circ \pm 6^\circ$. The IR and optical observations and data analysis, as well as the host-galaxy modeling, are described in Appendix B.

4. Implications for Particle Acceleration Scenarios

The spectral energy distribution of the synchrotron emission from 1ES 1959+650 typically peaks in the X-ray band (~0.1–100 keV; Chang et al. 2019). It belongs to the category of high-frequency-peaked BL Lac–type blazars, a subclass that includes Mrk 501 and Mrk 421, which exhibit the highest X-ray fluxes (Perlman et al. 1996). In a leptonic-dominated emission scenario, the IR to X-ray emission from these objects is attributed to synchrotron radiation produced by electrons (and possibly positrons) in the jet's magnetic field. Synchrotron radiation is inherently polarized, with a degree of polarization of $\Pi \sim 70\%$ for electrons in a homogeneous magnetic field. After correcting for relativistic aberration, the polarization angle (ψ) at optically thin wavelengths is perpendicular to the average magnetic field direction projected onto the plane of the sky. In the case of BL Lac–type blazars, observations typically show polarization degrees of $\Pi \lesssim 20\%$ (Jorstad et al. 2005; Smith et al. 2007; Hovatta et al. 2016; Blinov et al. 2021).

There are two main reasons for the reduction in observed polarization. First, geometrical depolarization occurs when there is a random component in the magnetic field with varying orientations within the emitting region. This geometrical depolarization effect becomes more pronounced as the ratio of random to ordered magnetic field (B_r/B_0) increases (Ginzburg & Syrovatskii 1965). Second, temporal depolarization happens when the magnetic field direction changes over timescales shorter than the integration time of the polarization measurement. The magnitude of this effect increases with the amplitude of unresolved changes in polarization angle (Di Gesu et al. 2022b; Zhang et al. 2022). This phenomenon was observed in IXPE observations of Mrk 421 (Di Gesu et al. 2023).

The degree of polarization in the X-ray band can be compared to that measured at optical frequencies during the same epoch. This polarization ratio Π_x/Π_O can be used as a diagnostic for potential differences in the magnetic field geometry and dynamics encountered by the populations of electrons responsible for the emission in each band. Previous IXPE observations of Mrk 501 and Mrk 421 have shown higher X-ray polarization compared to optical and radio frequencies (Di Gesu et al. 2022a; Liodakis et al. 2022), which can be explained by an energy-stratified particle distribution that would naturally arise in shock acceleration scenarios (e.g., Tavecchio et al. 2018).

On 2022 May 3–4, the ratio of X-ray to optical degree of polarization in 1ES 1959+650 was measured to be $\Pi_x/\Pi_O = 1.8 \pm 0.5$, lower than observed in Mrk 421 ($\Pi_x/\Pi_O \sim 5$; Di Gesu et al. 2022a) and comparable to Mrk 501 ($\Pi_x/\Pi_O \sim 2.5$; Liodakis et al. 2022). As in Mrk 501, the X-ray and optical polarization angles of 1ES 1959+650 were aligned (within 30°) with the jet direction, inferred to be $\phi \sim 150^\circ$ from VLBA images (Piner et al. 2010; Weaver et al. 2022; Figure 4), indicating a magnetic field geometry consistent with a helical

[69] https://people.bu.edu/clemens/mimir/index.html

or toroidal configuration (Hovatta et al. 2012) or compression by a shock (Hughes et al. 1985).

In contrast, during the second IXPE exposure on 2022 June 9–12, the average optical polarization was $\Pi_O = 5.4\% \pm 1.1\%$, while the X-ray polarization was $\Pi_x < 5.1\%$ (Figure 3), suggesting $\Pi_x/\Pi_o \lesssim 1.0$. The optical polarization angle exhibited a rotation from $\psi_O \gtrsim 170°$ 1 day before June 9–12 to 103° during the IXPE exposure, returning to ∼160° 5 days after (Figure 2). Similar polarization angle excursions were observed in 2013–2016 (Blinov et al. 2021). IR observations also indicated a change in polarization angle during the second IXPE exposure. The X-ray flux exhibited smooth variations with a peak-to-valley amplitude of approximately 50% of the median X-ray flux (Figure 2).

Various single-zone models can explain the observed depolarization as geometrical. In shock acceleration scenarios, energy-dependent geometrical depolarization arises as electrons with decreasing energies occupy a larger volume, leading to a higher random magnetic field component and increased geometrical depolarization toward lower frequencies (Angelakis et al. 2016; Tavecchio et al. 2018; Liodakis et al. 2022). In magnetic reconnection scenarios, geometrical depolarization can occur due to the increasing range of magnetic field orientations as high-energy electrons move away from X-points where the highly ordered magnetic field changes direction (Tchekhovskoy et al. 2009; Sironi & Spitkovsky 2014). However, a precise calculation of the X-ray versus optical polarization degree is not straightforward. The presence of a kink instability can create preferred locations for current sheets, and if the reconnecting fields are mainly toroidal (Zhang et al. 2022), the emitted radiation should exhibit a polarization angle roughly aligned with the jet axis.

Multizone models with turbulent magnetic field cells predict greater geometrical depolarization at optical frequencies than at X-ray energies (Marscher 2014). However, in such models it is the *mean* X-ray polarization that should exceed the *mean* optical polarization by a factor of $\gtrsim 2$ (Marscher & Jorstad 2022). Temporal fluctuations of both, with a standard deviation equal to 0.5 times the mean, are expected, so the Π_X/Π_O ratio should vary over time. Turbulence-based models also predict polarization angle swings that are not associated with changes in flux or polarization degree (Zhang et al. 2023).

5. Conclusions

On 2022 May 3–4, IXPE detected X-ray polarization from the BL Lac–type blazar 1ES 1959+650. The degree of polarization in the 2–8 keV band was measured to be $\Pi_x = 8.0 \pm 2.3$, with an electric-vector polarization position angle $\psi_x = 123° \pm 8°$. Bharathan et al. (2023) do not report a significant detection of X-ray polarization from this data set, possibly due to their use of a model-independent analysis that is less sensitive than the spectropolarimetric analysis presented here. Our study constrains the degree of polarization during a second IXPE exposure on 2022 June 9–12 to $\Pi_x < 5.1\%$. Subsequent observations of 1ES 1959+650 with IXPE in 2022 October and 2023 August reveal increased X-ray polarization levels, reaching $\Pi_x = 12.5 \pm 0.7$ (Bharathan et al. 2023), compared to the levels from the earlier campaign reported here.

A time-resolved analysis of the second data set shows significant polarization during one of four 50 ks time bins, with a polarization degree and angle compatible with the May 3–4 observation. Considering the measurement uncertainties, the hypothesis of a constant Π_x over the two observations can be only marginally rejected at a 2.3σ confidence level.

During the 50 day period including the two IXPE observations, optical polarization measurements showed a range of $2.3\% \leqslant \Pi_O \leqslant 6.5\%$, with a median value of 3.9%. When comparing the degree of polarization between the X-ray and optical bands, a ratio of $\Pi_x/\Pi_O = 1.8 \pm 0.5$ was observed during May 3–4, while $\Pi_x/\Pi_O \lesssim 1.0$ was observed during June 9–12.

The amplitude of the galaxy-subtracted optical flux variability was 35% (peak to valley) during the campaign, while the X-ray flux changed by a factor of ∼3. Although the optical and IR position angles of polarization varied significantly during the second IXPE pointing, the degree of polarization in these bands remained low, at around 4%. This suggests the presence of multiple magnetic field directions within the optical and IR emission regions, which could be a result of turbulence or magnetic reconnection events.

Recent observations of nearby high-frequency-peaked BL Lacs (Mrk 501 and Mrk 421; $z \sim 0.03$) at X-ray and optical frequencies have shown a higher degree of polarization in the X-ray band. This has been interpreted as evidence for an energy-stratified electron population dominating the observed radiative output of the jet (Di Gesu et al. 2022a; Liodakis et al. 2022). Similar results have been obtained with analogs of those objects at higher redshift (PG 1553+113, $z \sim 0.4$; 1ES 0229 +200, $z = 0.140$; Middei et al. 2023b; Ehlert et al. 2023).

Our observations of 1ES 1959+650 represent the first time that X-ray polarization is detected from a high-frequency-peaked BL Lac without clearly exhibiting frequency dependence. The observed ratio $\Pi_x/\Pi_o \lesssim 1.0$ in 1ES 1959 +650 during the second IXPE pointing is in apparent contradiction with a scenario where electrons emitting optical radiation occupy a larger volume with a more turbulent magnetic field compared to the higher-energy electrons responsible for the X-ray emission. Nevertheless, the higher-amplitude flux variability in the X-ray band compared to that at optical frequencies suggests a more compact X-ray-emitting region.

Temporal depolarization induced by turbulence in the X-ray-emitting region could potentially explain occasions when the observed X-ray and optical polarization becomes $\Pi_X \approx \Pi_O$. If changes in polarization angle occur on timescales shorter than the 50 ks resolution of IXPE at the observed flux levels, the degree of polarization in the X-ray band will be suppressed. Optical observations, with integration times of $\lesssim 2$ ks, are less susceptible to temporal depolarization caused by slowly varying magnetic field configurations.

The change in optical polarization angle observed during the second IXPE pointing, in the absence of significant X-ray or optical flux variability, could be explained by multizone emission from turbulent plasma cells with typical dynamical timescales of <1 day. However, models based on turbulence alone do not predict the alignment of the electric-vector polarization angle with the projected jet axis direction. During this campaign, we observed $\psi_x \approx \psi_o$ aligned within 30° of the projected jet direction, as measured with the VLBA. Models in which turbulent plasma crosses a shock have the potential to explain alignment with the jet as well as the time variability (Marscher 2014; Tavecchio et al. 2018; Tavecchio 2021).

A plausible alternative explanation for the lower degree of X-ray polarization measured in 1ES 1959+650 compared to Mrk 501 and Mrk 421 could be a minor contribution from the rising edge of the high-energy emission component of the spectral energy distribution to the observed 2–8 keV X-ray flux. This second emission component consists of Compton-scattered photons that are expected to have a very low degree of polarization (Krawczynski 2012). Thus, their presence in the IXPE data would weaken the measured degree of X-ray polarization in that band. Despite the absence of spectral curvature in the Swift-XRT and XMM-Newton spectral models, uncertainties might allow for a slight contribution from Compton-scattered emission at the highest energies. However, it is worth noting that no significant (inverted) spectral break, which would indicate a second spectral X-ray component, was indicated in the model fitting.

Given the time variability of the flux and polarization, further IXPE and multiwavelength polarization and flux monitoring observations of 1ES 1959+650 are needed to probe the magnetic field geometry and the relationship between the emission regions at X-ray, optical, and IR wavelengths. During our campaign, the influence of geometrical and temporal depolarization cannot be fully distinguished. At X-ray flux levels of $F_{2-8\,\mathrm{keV}} = 10^{-10}$ erg cm^{-2} s^{-1} and $\Pi_x \sim 8\%$, IXPE has the capability to detect changes in the polarization degree within approximately 50 ks. The sensitivity of IXPE scales as $\mathrm{MDP}_{99} \propto (\mathtt{exposure} \times F_{2-8\,\mathrm{keV}})^{-1/2}$, indicating that variations in X-ray polarization down to levels of $\Pi_x \lesssim 5\%$ could be resolved when the X-ray flux from 1ES 1959+650 is $F_{2-8\,\mathrm{keV}} \gtrsim 3 \times 10^{-10}$ erg cm^{-2} s^{-1}, or approximately twice as bright as the flux levels during the reported campaign. This capability has been demonstrated recently with the detection by IXPE of a $>360°$ X-ray polarization angle rotation in Mrk 421 (Di Gesu et al. 2023).

Acknowledgments

The authors thank Alex Chen for useful discussions on the expectations for a polarized flux arising from magnetic reconnection events. The Imaging X-ray Polarimetry Explorer (IXPE) is a joint US and Italian mission. The US contribution is supported by the National Aeronautics and Space Administration (NASA) and led and managed by its Marshall Space Flight Center (MSFC), with industry partner Ball Aerospace (contract NNM15AA18C). The Italian contribution is supported by the Italian Space Agency (Agenzia Spaziale Italiana, ASI) through contract ASI-OHBI-2017-12-I.0, agreements ASI-INAF-2017-12-H0 and ASI-INFN-2017.13-H0, and its Space Science Data Center (SSDC), and by the Istituto Nazionale di Astrofisica (INAF) and the Istituto Nazionale di Fisica Nucleare (INFN) in Italy. This research used data products provided by the IXPE Team (MSFC, SSDC, INAF, and INFN) and distributed with additional software tools by the High-Energy Astrophysics Science Archive Research Center (HEASARC), at NASA Goddard Space Flight Center (GSFC). We acknowledge financial support from ASI-INAF agreement No. 2022-14-HH.0. I.L. was supported by the NASA Postdoctoral Program at the Marshall Space Flight Center, administered by Oak Ridge Associated Universities under contract with NASA. The research at Boston University was supported in part by National Science Foundation grant AST-2108622 and by NASA Swift Guest Investigator grant 80NSSC22K0537 and Fermi Guest Investigator grants 80NSSC21K1917 and 80NSSC22K1571. This research has made use of data from the RoboPol program, a collaboration between Caltech, the University of Crete, IA-FORTH, IUCAA, the MPIfR, and the Nicolaus Copernicus University, which was conducted at Skinakas Observatory in Crete, Greece. The IAA-CSIC coauthors acknowledge financial support from the Spanish "Ministerio de Ciencia e Innovación" (MCIN/AEI/ 10.13039/501100011033) through the Center of Excellence Severo Ochoa award for the Instituto de Astrofísica de Andalucía-CSIC (CEX2021-001131-S) and grants PID2019-107847RB-C44 and PID2022-139117NB-C44. Some of the data are based on observations collected at the Observatorio de Sierra Nevada, owned and operated by the Instituto de Astrofísica de Andalucía (IAA-CSIC). Further data are based on observations collected at the Centro Astronómico Hispano-Alemán (CAHA), operated jointly by Junta de Andalucía and Consejo Superior de Investigaciones Científicas (IAA-CSIC). The POLAMI observations were carried out at the IRAM 30 m telescope. IRAM is supported by INSU/CNRS (France), MPG (Germany), and IGN (Spain). The data in this study include observations made with the Nordic Optical Telescope, owned in collaboration by the University of Turku and Aarhus University and operated jointly by Aarhus University, the University of Turku, and the University of Oslo, representing Denmark, Finland, and Norway; the University of Iceland; and Stockholm University at the Observatorio del Roque de los Muchachos, La Palma, Spain, of the Instituto de Astrofisica de Canarias. The data presented here were obtained in part with ALFOSC, which is provided by the Instituto de Astrofísica de Andalucía (IAA) under a joint agreement with the University of Copenhagen and NOT. E.L. was supported by Academy of Finland projects 317636 and 320045. This study was based in part on observations conducted using the Perkins Telescope Observatory (PTO) in Arizona, USA, which is owned and operated by Boston University. We acknowledge funding to support our NOT observations from the Finnish Centre for Astronomy with ESO (FINCA), University of Turku, Finland (Academy of Finland grant No. 306531). Part of the French contribution is supported by the Scientific Research National Center (CNRS) and the French Spatial Agency (CNES). D.B., S.K., R.S., and N.M. acknowledge support from the European Research Council (ERC) under the European Union's Horizon 2020 research and innovation program under grant agreement No. 771282. C.C. acknowledges support by the European Research Council (ERC) under the HORIZON ERC grants 2021 program under grant agreement No. 101040021.

The VLBA is an instrument of the National Radio Astronomy Observatory. The National Radio Astronomy Observatory is a facility of the National Science Foundation operated under cooperative agreement by Associated Universities, Inc. This work was supported by JST, the establishment of university fellowships toward the creation of science technology innovation, grant No. JPMJFS2129. This work was supported by Japan Society for the Promotion of Science (JSPS) KAKENHI grant No. JP21H01137. This work was also partially supported by the Optical and Near-Infrared Astronomy Inter-University Cooperation Program from the Ministry of Education, Culture, Sports, Science and Technology (MEXT) of Japan. We are grateful to the observation and operating members of the Kanata Telescope. The Submillimeter Array is a joint project between the Smithsonian Astrophysical Observatory and the Academia Sinica Institute

of Astronomy and Astrophysics and is funded by the Smithsonian Institution and the Academia Sinica. Maunakea, the location of the SMA, is a culturally important site for the indigenous Hawaiian people; we are privileged to study the cosmos from its summit.

Facility: CAO, IRAM-30m, IXPE, KANATA, NOT, Perkins, SNO, Skinakas, SMA, VLBA, Swift-XRT, XMM-Newton.

Software: astropy (Astropy Collaboration et al. 2013, 2018, 2022), Sherpa (Freeman et al. 2001), `Xspec` (Arnaud 1996), `ixpeobssim` (Baldini et al. 2022a, 2022b), HEASoft (NASA High Energy Astrophysics Science Archive Research Center (HEASARC) 2014), SAS (Gabriel et al. 2004).

Appendix A
X-Ray Data Reduction

A.1. IXPE

Level 2 IXPE event files containing Stokes parameters calculated on an event-by-event basis were downloaded from the public `HEASARC` data repository. Data were further processed using `ixpeobssim v30.2.2` (Baldini et al. 2022a, 2022b). Signal events were extracted using the `xpselect` tool from an 80″ radius circle centered on the sky location of 1ES 1959+650. Background photon counts were extracted from an annulus with an inner radius of 140″ and outer radius of 200″ centered on the same location. This procedure was repeated for each of the three IXPE detector units (DU1–3; Weisskopf et al. 2022). Spectra were background-dominated at energies above 6 keV. Stokes I, Q, and U spectra in the 2–6 keV band were therefore extracted using `xpbin` without using event weights and binned to a minimum of 8 counts per bin. Spectropolarimetric analysis was performed using `Sherpa v4.14` (Burke et al. 2022), with custom spectropolarimetry models equivalent to the `polconst` models found in `Xspec`. For June 9–12, the constant associated with XMM-Newton is 0.82 and that of Swift-XRT is 1.35, while those for detector units DU2 and DU3 are 0.97 and 0.92, all normalized to IXPE DU1. The wider spread in intercalibration constants can be attributed to the X-ray flux variability of 1ES 1959+650 during and after June 9–12.

A.2. Swift-XRT

Swift-XRT observations were performed in both photon counting and windowed timing mode. Files were processed using `xrtpipeline` packaged in `HEASoft v6.30` using the latest Swift-XRT calibration files. Signal events were extracted from a 60″ radius circle centered on 1ES 1959+650. Background photon counts were extracted from an annulus with an inner radius of 150″ and outer radius of 280″. Spectra were binned to have at least 40 counts per energy bin and fit using `Xspec` (Arnaud 1996) to extract fluxes and spectral information.

A.3. XMM-Newton

XMM-Newton observations were performed with the pn camera in timing mode, using the thick filter to mitigate pileup effects. EPAT plots clearly indicated the presence of pileup in the MOS cameras, rendering the MOS data unsuitable for analysis. Spectra were generated using version `20210317_1624-19.1.0` of the XMM-Newton Science Analysis Software (SAS) and the latest calibration products. To derive the spectrum of the source, a 27 pixel size box was employed, centered on the source itself. For background extraction, a region of the same size was selected from a blank area on the EPIC-pn CCD camera. To ensure accurate analysis, the resulting spectrum was appropriately rebinned to achieve a minimum of 30 counts per bin. Moderate pileup was observed in the pn data below 1 keV, prompting the restriction of spectral analysis to the 1.0–10 keV energy range. After background subtraction, the net exposure in the pn camera is 1.39×10^4 s.

Appendix B
Infrared/Optical Observations and Data Reduction

B.1. Infrared Observations

The IR observations were obtained with the MIMIR instrument at the 1.8 m PTO in Flagstaff, Arizona. A detailed description of the camera and data reduction can be found in Clemens et al. (2012). One observation was the result of six dithering exposures of 10 s each at 16 positions of a half-wave plate, rotated in steps of 22.°5 from 0° to 360°. Therefore, to determine the polarization parameters at a given epoch, we collected 96 measurements of the source. We carried out 15 and 10 observations in the H and K bands, respectively, from MJD 59736.5 to MJD 59748.5. To perform photometry, we have coadded all 96 exposures at a given epoch to construct a deep image. These deep images were also used to model the host galaxy of 1959+650 in the H and K bands.

To make a model of the host galaxy, we used a photometric decomposition technique, which allows one to find an analytical model of an object and separate the light coming from its components. The distance to the object does not allow us to resolve it in great detail on our IR images, so in this work, we adopted a rather simple model consisting of two components: a Sérsic (Sérsic 1963, 1968) function to describe the host galaxy and a point source for the active nucleus. We built the point-spread function (PSF) by averaging images of bright, isolated, and unsaturated stars and fit the resulting image with a Moffat function (Moffat 1969) to produce a smooth image. To run the decomposition, we used the IMFIT package (Erwin 2015). Our estimates of the host-galaxy structural parameters are as follows: ellipticity $e = 0.31 \pm 0.05$, position angle $\mathrm{PA} = 72.°9 \pm 13.°1$, Sérsic index $n = 1.55 \pm 0.5$, effective radius $r_e(K) = 2.53 \pm 0.''46$, $r_e(H) = 2.84 \pm 0.''35$, effective surface brightness $\mu_e(K) = 16.98 \pm 0.''39$, and $\mu_e(H) = 17.65 \pm 0.''27$ mag arcsec^{-2}. The rather large uncertainties, especially in the Sérsic index value, are attributed to poor resolution of the object; the observed object effective radius is close to the PSF FWHM, which results in a degradation of the decomposition quality (Trujillo et al. 2001). We have employed the model parameters to estimate the contributions of the host galaxy of 1959+650 within an aperture of diameter 5″ that are equal to 14.28 ± 0.09 and 13.71 ± 0.05 mag in the H and K bands, respectively.

B.2. Optical Observations

The optical R-band observations were performed at the Calar Alto Observatory, the KANATA telescope, the NOT using the Alhambra Faint Object Spectrograph and Camera (ALFOSC), the Sierra Nevada Observatory, and the Skinakas Observatory using the RoboPol polarimeter. The Calar Alto and SNO observations were obtained on 2022 June 6, 10, and 17

(MJD 59737.1, 59740.9, 59741.0, and 59747.8) and analyzed using standard photopolarimetric procedures. The KANATA observations were obtained on 2022 May 3 (MJD 59702.0) using the Hiroshima Optical and Near-InfraRed camera (Kawabata et al. 1999; Akitaya et al. 2014) and analyzed using standard procedures. The NOT observations were obtained on 2022 May 4 (MJD 59703.1) and 2022 June 7 (MJD 59737.1). The data were analyzed using unpolarized and polarized standard stars for calibration, following the standard photometric procedures included in the Tuorla Observatory pipeline (Hovatta et al. 2016; Nilsson et al. 2018). The RoboPol polarimeter is a novel four-channel polarimeter that simultaneously measures Π_O and ψ_O with a single exposure (Ramaprakash et al. 2019). Details of the analysis pipeline and data reduction procedures can be found in Panopoulou et al. (2015) and Blinov et al. (2021).

All of the optical observations were corrected for the depolarization effect of unpolarized host-galaxy contribution to the emission following Nilsson et al. (2007). A more detailed description of the analysis procedures from the different observatories can be found in Di Gesu et al. (2022a), Liodakis et al. (2022), and Middei et al. (2023a).

ORCID iDs

Manel Errando https://orcid.org/0000-0002-1853-863X
Ioannis Liodakis https://orcid.org/0000-0001-9200-4006
Alan P. Marscher https://orcid.org/0000-0001-7396-3332
Herman L. Marshall https://orcid.org/0000-0002-6492-1293
Michela Negro https://orcid.org/0000-0002-6548-5622
Abel Lawrence Peirson https://orcid.org/0000-0001-6292-1911
Matteo Perri https://orcid.org/0000-0003-3613-4409
Simonetta Puccetti https://orcid.org/0000-0002-2734-7835
Pazit L. Rabinowitz https://orcid.org/0000-0002-5104-5263
Iván Agudo https://orcid.org/0000-0002-3777-6182
Svetlana G. Jorstad https://orcid.org/0000-0001-6158-1708
Ioakeim G. Bourbah https://orcid.org/0000-0002-8597-6154
Sebastian Kiehlmann https://orcid.org/0000-0001-6314-9177
Nikos Mandarakas https://orcid.org/0000-0002-2567-2132
Anna Vervelaki https://orcid.org/0000-0003-0271-9724
Giacomo Bonnoli https://orcid.org/0000-0003-2464-9077
Beatriz Agís-González https://orcid.org/0000-0001-7702-8931
César Husillos https://orcid.org/0000-0001-8286-5443
Alessandro Marchini https://orcid.org/0000-0003-3779-6762
Alfredo Sota https://orcid.org/0000-0002-9404-6952
Pouya M. Kouch https://orcid.org/0000-0002-9328-2750
Juan Escudero https://orcid.org/0000-0002-4131-655X
Ioannis Myserlis https://orcid.org/0000-0003-3025-9497
Tsunefumi Mizuno https://orcid.org/0000-0001-7263-0296
Hiroshi Akitaya https://orcid.org/0000-0001-6156-238X
Mark Gurwell https://orcid.org/0000-0003-0685-3621
Garrett K. Keating https://orcid.org/0000-0002-3490-146X
Adam Ingram https://orcid.org/0000-0002-5311-9078
Francesco Massaro https://orcid.org/0000-0002-1704-9850
Lucio Angelo Antonelli https://orcid.org/0000-0002-5037-9034
Raffaella Bonino https://orcid.org/0000-0002-4264-1215
Elisabetta Cavazzuti https://orcid.org/0000-0001-7150-9638
Chien-Ting Chen https://orcid.org/0000-0002-4945-5079
Nicolò Cibrario https://orcid.org/0000-0003-3842-4493
Stefano Ciprini https://orcid.org/0000-0002-0712-2479
Alessandra De Rosa https://orcid.org/0000-0001-5668-6863
Laura Di Gesu https://orcid.org/0000-0002-5614-5028
Immacolata Donnarumma https://orcid.org/0000-0002-4700-4549
Steven R. Ehlert https://orcid.org/0000-0003-4420-2838
Ephraim Gau https://orcid.org/0000-0002-5250-2710
Vladimir Karas https://orcid.org/0000-0002-5760-0459
Dawoon E. Kim https://orcid.org/0000-0001-5717-3736
Henric Krawczynski https://orcid.org/0000-0002-1084-6507
Marco Laurenti https://orcid.org/0000-0001-5762-6360
Lindsey Lisalda https://orcid.org/0000-0002-5202-1642
Frédéric Marin https://orcid.org/0000-0003-4952-0835
Andrea Marinucci https://orcid.org/0000-0002-2055-4946
Fabio Muleri https://orcid.org/0000-0003-3331-3794
Pierre-Olivier Petrucci https://orcid.org/0000-0001-6061-3480
Nicole Rodriguez Cavero https://orcid.org/0000-0001-5256-0278
Roger W. Romani https://orcid.org/0000-0001-6711-3286
Fabrizio Tavecchio https://orcid.org/0000-0003-0256-0995
Stefano Tugliani https://orcid.org/0000-0002-3318-9036
Kinwah Wu https://orcid.org/0000-0002-7568-8765
Matteo Bachetti https://orcid.org/0000-0002-4576-9337
Luca Baldini https://orcid.org/0000-0002-9785-7726
Wayne H. Baumgartner https://orcid.org/0000-0002-5106-0463
Ronaldo Bellazzini https://orcid.org/0000-0002-2469-7063
Stefano Bianchi https://orcid.org/0000-0002-4622-4240
Stephen D. Bongiorno https://orcid.org/0000-0002-0901-2097
Alessandro Brez https://orcid.org/0000-0002-9460-1821
Niccolò Bucciantini https://orcid.org/0000-0002-8848-1392
Fiamma Capitanio https://orcid.org/0000-0002-6384-3027
Simone Castellano https://orcid.org/0000-0003-1111-4292
Enrico Costa https://orcid.org/0000-0003-4925-8523
Ettore Del Monte https://orcid.org/0000-0002-3013-6334
Niccolò Di Lalla https://orcid.org/0000-0002-7574-1298
Alessandro Di Marco https://orcid.org/0000-0003-0331-3259
Victor Doroshenko https://orcid.org/0000-0001-8162-1105
Michal Dovčiak https://orcid.org/0000-0003-0079-1239
Teruaki Enoto https://orcid.org/0000-0003-1244-3100
Yuri Evangelista https://orcid.org/0000-0001-6096-6710
Sergio Fabiani https://orcid.org/0000-0003-1533-0283
Riccardo Ferrazzoli https://orcid.org/0000-0003-1074-8605
Javier A. Garcia https://orcid.org/0000-0003-3828-2448
Shuichi Gunji https://orcid.org/0000-0002-5881-2445
Jeremy Heyl https://orcid.org/0000-0001-9739-367X
Wataru Iwakiri https://orcid.org/0000-0002-0207-9010
Philip Kaaret https://orcid.org/0000-0002-3638-0637
Fabian Kislat https://orcid.org/0000-0001-7477-0380
Jeffery J. Kolodziejczak https://orcid.org/0000-0002-0110-6136
Fabio La Monaca https://orcid.org/0000-0001-8916-4156
Luca Latronico https://orcid.org/0000-0002-0984-1856

Simone Maldera https://orcid.org/0000-0002-0698-4421
Alberto Manfreda https://orcid.org/0000-0002-0998-4953
Giorgio Matt https://orcid.org/0000-0002-2152-0916
C.-Y. Ng https://orcid.org/0000-0002-5847-2612
Stephen L. O'Dell https://orcid.org/0000-0002-1868-8056
Nicola Omodei https://orcid.org/0000-0002-5448-7577
Chiara Oppedisano https://orcid.org/0000-0001-6194-4601
Alessandro Papitto https://orcid.org/0000-0001-6289-7413
George G. Pavlov https://orcid.org/0000-0002-7481-5259
Melissa Pesce-Rollins https://orcid.org/0000-0003-1790-8018
Maura Pilia https://orcid.org/0000-0001-7397-8091
Andrea Possenti https://orcid.org/0000-0001-5902-3731
Juri Poutanen https://orcid.org/0000-0002-0983-0049
Brian D. Ramsey https://orcid.org/0000-0003-1548-1524
John Rankin https://orcid.org/0000-0002-9774-0560
Ajay Ratheesh https://orcid.org/0000-0003-0411-4243
Oliver J. Roberts https://orcid.org/0000-0002-7150-9061
Carmelo Sgrò https://orcid.org/0000-0001-5676-6214
Patrick Slane https://orcid.org/0000-0002-6986-6756
Paolo Soffitta https://orcid.org/0000-0002-7781-4104
Gloria Spandre https://orcid.org/0000-0003-0802-3453
Douglas A. Swartz https://orcid.org/0000-0002-2954-4461
Toru Tamagawa https://orcid.org/0000-0002-8801-6263
Roberto Taverna https://orcid.org/0000-0002-1768-618X
Allyn F. Tennant https://orcid.org/0000-0002-9443-6774
Nicholas E. Thomas https://orcid.org/0000-0003-0411-4606
Francesco Tombesi https://orcid.org/0000-0002-6562-8654
Alessio Trois https://orcid.org/0000-0002-3180-6002
Sergey S. Tsygankov https://orcid.org/0000-0002-9679-0793
Roberto Turolla https://orcid.org/0000-0003-3977-8760
Jacco Vink https://orcid.org/0000-0002-4708-4219
Martin C. Weisskopf https://orcid.org/0000-0002-5270-4240
Fei Xie https://orcid.org/0000-0002-0105-5826
Silvia Zane https://orcid.org/0000-0001-5326-880X

References

Agudo, I., Thum, C., Molina, S. N., et al. 2018b, MNRAS, 474, 1427
Agudo, I., Thum, C., Ramakrishnan, V., et al. 2018a, MNRAS, 473, 1850
Akitaya, H., Moritani, Y., Ui, T., et al. 2014, Proc. SPIE, 9147, 91474O
Aliu, E., Archambault, S., Arlen, T., et al. 2013, ApJ, 775, 3
Aliu, E., Archambault, S., Arlen, T., et al. 2014, ApJ, 797, 89
Angel, J. R. P., & Stockman, H. S. 1980, ARA&A, 18, 321
Angelakis, E., Hovatta, T., Blinov, D., et al. 2016, MNRAS, 463, 3365
Arnaud, K. A. 1996, in ASP Conf. Ser. 101, Astronomical Data Analysis Software and Systems V, ed. G. H. Jacoby & J. Barnes (San Francisco, CA: ASP), 17
Astropy Collaboration, Price-Whelan, A. M., Lim, P. L., et al. 2022, ApJ, 935, 167
Astropy Collaboration, Price-Whelan, A. M., Sipőcz, B. M., et al. 2018, AJ, 156, 123
Astropy Collaboration, Robitaille, T. P., Tollerud, E. J., et al. 2013, A&A, 558, A33
Baldini, L., Bucciantini, N., Lalla, N. D., et al. 2022a, SoftX, 19, 101194
Baldini, L., Bucciantini, N., Lalla, N. D., et al., 2022b ixpeobssim: Imaging X-ray Polarimetry Explorer simulator and analyzer, Astrophysics Source Code Library, ascl:2210.020
Begelman, M. C., Blandford, R. D., & Rees, M. J. 1984, RvMP, 56, 255
Bharathan, A. M., Stalin, C. S., Chatterjee, R., et al. 2023, arXiv:2311.01745
Blandford, R., Meier, D., & Readhead, A. 2019, ARA&A, 57, 467
Blandford, R. D., & Ostriker, J. P. 1978, ApJL, 221, L29
Blandford, R. D., & Znajek, R. L. 1977, MNRAS, 179, 433
Blinov, D., Kiehlmann, S., Pavlidou, V., et al. 2021, MNRAS, 501, 3715
Bodo, G., Tavecchio, F., & Sironi, L. 2021, MNRAS, 501, 2836
Burke, D., Laurino, O., Günther, H. M., et al. 2022, sherpa/sherpa: Sherpa v4.15.0, Zenodo, 10.5281/zenodo.7186379
Burrows, D. N., Hill, J. E., Nousek, J. A., et al. 2005, SSRv, 120, 165
Chang, Y. L., Arsioli, B., Giommi, P., Padovani, P., & Brandt, C. H. 2019, A&A, 632, A77
Clemens, D. P., Pinnick, A. F., & Pavel, M. D. 2012, ApJS, 200, 20
Dermer, C. D., Miller, J. A., & Li, H. 1996, ApJ, 456, 106
de Vaucouleurs, G., de Vaucouleurs, A., Corwin, H. G. J., et al. 1991, Third Reference Catalogue of Bright Galaxies (New York: Springer)
Di Gesu, L., Donnarumma, I., Tavecchio, F., et al. 2022a, ApJL, 938, L7
Di Gesu, L., Marshall, H. L., Ehlert, S. R., et al. 2023, NatAs, 7, 1245
Di Gesu, L., Tavecchio, F., Donnarumma, I., et al. 2022b, A&A, 662, A83
Ehlert, S. R., Liodakis, I., Middei, R., et al. 2023, ApJ, 959, 61
Erwin, P. 2015, ApJ, 799, 226
Falcke, H., Körding, E., & Markoff, S. 2004, A&A, 414, 895
Freeman, P., Doe, S., & Siemiginowska, A. 2001, Proc. SPIE, 4477, 76
Gabriel, C., Denby, M., Fyfe, D. J., et al. 2004, in ASP Conf. Ser. 314, Astronomical Data Analysis Software and Systems XIII, ed. F. Ochsenbein, M. G. Allen, & D. Egret (San Francisco, CA: ASP), 759
Ginzburg, V. L., & Syrovatskii, S. I. 1965, ARA&A, 3, 297
Giommi, P., Polenta, G., Lähteenmäki, A., et al. 2012, A&A, 541, A160
HI4PI Collaboration, Ben Bekhti, N., Flöer, L., et al. 2016, A&A, 594, A116
Holder, J., Bond, I. H., Boyle, P. J., et al. 2003, ApJL, 583, L9
Hovatta, T., Lindfors, E., Blinov, D., et al. 2016, A&A, 596, A78
Hovatta, T., Lister, M. L., Aller, M. F., et al. 2012, AJ, 144, 105
Hughes, P. A., Aller, H. D., & Aller, M. F. 1985, ApJ, 298, 301
Hughes, P. A., & Bregman, J. N. 2006, in AIP Conf. Ser. 856, Relativistic Jets: The Common Physics of AGN, Microquasars, and Gamma-Ray Bursts, 856, ed. P. A. Hughes & J. N. Bregman (Melville, NY: AIP)
Jorstad, S. G., Marscher, A. P., Lister, M. L., et al. 2005, AJ, 130, 1418
Jorstad, S. G., Marscher, A. P., Morozova, D. A., et al. 2017, ApJ, 846, 98
Kagan, D., Sironi, L., Cerutti, B., & Giannios, D. 2015, SSRv, 191, 545
Kapanadze, B., Romano, P., Vercellone, S., Kapanadze, S., & Kharshiladze, G. 2014, Proc. Swift: 10 Years of Discovery, 10, 142
Katarzyński, K., Ghisellini, G., Mastichiadis, A., Tavecchio, F., & Maraschi, L. 2006, A&A, 453, 47
Kawabata, K. S., Okazaki, A., Akitaya, H., et al. 1999, PASP, 111, 898
Kirk, J. G., Duffy, P., & Gallant, Y. A. 1996, A&A, 314, 1010
Krawczynski, H. 2012, ApJ, 744, 30
Krawczynski, H., Hughes, S. B., Horan, D., et al. 2004, ApJ, 601, 151
Liodakis, I., Marscher, A. P., Agudo, I., et al. 2022, Natur, 611, 677
Liodakis, I., Peirson, A. L., & Romani, R. W. 2019, ApJ, 880, 29
Lyubarsky, Y. E. 2010, MNRAS, 402, 353
Madsen, K. K., Beardmore, A. P., Forster, K., et al. 2017, AJ, 153, 2
Marrone, D. P., & Rao, R. 2008, Proc. SPIE, 7020, 70202B
Marscher, A. P. 2014, ApJ, 780, 87
Marscher, A. P., & Jorstad, S. G. 2021, Galax, 9, 27
Marscher, A. P., & Jorstad, S. G. 2022, Univ, 8, 644
Middei, R., Liodakis, I., Perri, M., et al. 2023a, ApJL, 942, L10
Middei, R., Perri, M., Puccetti, S., et al. 2023b, ApJL, 953, L28
Moffat, A. F. J. 1969, A&A, 3, 455
NASA High Energy Astrophysics Science Archive Research Center (HEASARC), 2014 HEAsoft: Unified Release of FTOOLS and XANADU, Astrophysics Source Code Library, ascl:1408.004
Nilsson, K., Lindfors, E., Takalo, L. O., et al. 2018, A&A, 620, A185
Nilsson, K., Pasanen, M., Takalo, L. O., et al. 2007, A&A, 475, 199
Nishikawa, K. I., Hardee, P., Richardson, G., et al. 2003, ApJ, 595, 555
Panopoulou, G., Tassis, K., Blinov, D., et al. 2015, MNRAS, 452, 715
Perlman, E. S., Stocke, J. T., Schachter, J. F., et al. 1996, ApJS, 104, 251
Piner, B. G., Pant, N., & Edwards, P. G. 2010, ApJ, 723, 1150
Primiani, R. A., Young, K. H., Young, A., et al. 2016, JAI, 5, 1641006
Ramaprakash, A. N., Rajarshi, C. V., Das, H. K., et al. 2019, MNRAS, 485, 2355
Romanova, M. M., & Lovelace, R. V. E. 1992, A&A, 262, 26
Rybicki, G. B., & Lightman, A. P. 1979, Radiative Processes in Astrophysics (New York: Wiley)
Sérsic, J. L. 1963, BAAA, 6, 41
Sérsic, J. L. 1968, Atlas de Galaxias Australes (Cordoba: Observatorio Astronomico)
Sironi, L., Keshet, U., & Lemoine, M. 2015a, SSRv, 191, 519
Sironi, L., Petropoulou, M., & Giannios, D. 2015b, MNRAS, 450, 183
Sironi, L., & Spitkovsky, A. 2014, ApJL, 783, L21
Smith, P. S., Williams, G. G., Schmidt, G. D., Diamond-Stanic, A. M., & Means, D. L. 2007, ApJ, 663, 118
Stroh, M. C., & Falcone, A. D. 2013, ApJS, 207, 28

Strüder, L., Briel, U., Dennerl, K., et al. 2001, A&A, 365, L18
Tagliaferri, G., Foschini, L., Ghisellini, G., et al. 2008, ApJ, 679, 1029
Tavecchio, F. 2021, Galax, 9, 37
Tavecchio, F., Landoni, M., Sironi, L., & Coppi, P. 2018, MNRAS, 480, 2872
Tavecchio, F., Landoni, M., Sironi, L., & Coppi, P. 2020, MNRAS, 498, 599
Tchekhovskoy, A., McKinney, J. C., & Narayan, R. 2009, ApJ, 699, 1789
Thum, C., Agudo, I., Molina, S. N., et al. 2018, MNRAS, 473, 2506
Trujillo, I., Aguerri, J. A. L., Cepa, J., & Gutiérrez, C. M. 2001, MNRAS, 328, 977
Urry, C. M., & Padovani, P. 1995, PASP, 107, 803
Vlahakis, N., & Königl, A. 2004, ApJ, 605, 656
Weaver, Z. R., Jorstad, S. G., Marscher, A. P., et al. 2022, ApJS, 260, 12
Weisskopf, M. C., Soffitta, P., Baldini, L., et al. 2022, JATIS, 8, 026002
Werner, G. R., Uzdensky, D. A., Begelman, M. C., Cerutti, B., & Nalewajko, K. 2018, MNRAS, 473, 4840
Zhang, H., Fang, K., Li, H., et al. 2019, ApJ, 876, 109
Zhang, H., Li, X., Giannios, D., et al. 2022, ApJ, 924, 90
Zhang, H., Marscher, A. P., Guo, F., et al. 2023, ApJ, 949, 71